https://doi.org/10.2352/ISSN.2470-1173.2017.17.COIMG-443

High-Resolution Image Reconstruction for PET Using Local and Non-local Regularizations

Xue Ren, Soo-Jin Lee; Electronic Engineering Department, Paichai University; Daejeon, Korea

Abstract

We present a maximum a posteriori (MAP) reconstruction method of increasing the pixel resolution of positron emission tomography (PET) whose typical pixel resolution is relatively low compared to that of other medical imaging modalities. We first model the underlying PET image on a finer grid and downsample it before performing forward projections to process with the observed low-resolution projection data at each iteration. We then apply a prior modeled by a linear combination of local and non-local regularizers to our MAP algorithm. The idea of combining the two different types of regularizers is based on our own notion that, while local regularizers are suitable for preserving fine-scale edges, non-local regularizers are suitable for preserving coarse-scale edges or flat regions. Our preliminary results show that the proposed method improves the reconstruction accuracy by compromising trade-offs of the two different types of regularization on a finer grid for high-resolution reconstruction.

Introduction

While positron emission tomography (PET) is recognized as one of the most advanced medical imaging techniques that can detect areas of molecular biology detail, it suffers from poor pixel resolution compared to magnetic resonance (MR) or X-ray computed tomography (CT) imaging. With the recent development of multimodal imaging systems, such as combined PET/CT and PET/MRI systems, increasing the resolution of PET images up to the level of the high-resolution CT or MR images has been of an important issue.

The purpose of this work is to increase the pixel resolution of PET images by incorporating a super-resolution (SR) technique into the reconstruction process. This study is related to the conventional SR technique that can enhance the resolution of an imaging system by using a single low-resolution (LR) image or a set of LR images, but is unique in that, unlike conventional imaging systems, the data formation process in PET is based on projections from a radiation source. In this case the reconstruction process involves projection and backprojection operations, which leads to a different approach to SR.

In this work we investigate a reconstruction method that can preserve fine-scale edges as well as coarse-scale edges of the underlying image while increasing the pixel resolution. We derive our reconstruction method within the context of a MAP approach where priors are designed to capture the spatial character of the underlying source. Unlike most common approaches that involve assumptions on the local spatial characteristics only, our method also include additional prior information derived from the non-local self-similarity property. By reflecting both local and non-local spatial characteristics in designing the prior, the resulting MAP reconstruction algorithm is expected to achieve a better accuracy on a finer grid for high-resolution reconstruction.

This paper is organized as follows. The Method section first shows how to increase the pixel resolution with a single frame projection data, and then describe how to combine the two types of priors and incorporate them into the MAP reconstruction process, and finally describes an optimization method to derive final update equations. The Results section describes our experimental results obtained from the simulation studies. The Conclusion section summarizes and draws our conclusion.

Method

In emission tomography reconstruction, the MAP approach is to estimate the underlying source image $\mathbf{f}$ from the emission measurement $\mathbf{g}$ by using the following minimization:

$$\hat{\mathbf{f}} = \arg\min_{\mathbf{f}} \left[-L(\mathbf{g}|\mathbf{f}) + \gamma R(\mathbf{f}) \right], \tag{1}$$

where $L(\mathbf{g}|\mathbf{f})$ is the likelihood term derived from the negative logarithm of the projection data given the underlying source image with the relationship $\mathbf{g}=H_1\mathbf{f}$, where H_1 is the system matrix, $R(\mathbf{f})$ is the negative log prior term, which is also known as the regularization term to penalize the image roughness, and γ is the smoothing parameter.

Since our method of enhancing the pixel resolution is related to the single-frame super-resolution (SFSR) method, we may derive our method in reference to the SFSR method.

For SFSR, there is only one observed low-resolution (LR) image for reconstruction. In this case the relationship between the observed LR image $\mathbf{f}_L$ and its corresponding high-resolution (HR) image $\mathbf{f}_H$ is given by

$$\mathbf{f}_L = DB\mathbf{f}_H, \tag{2}$$

where D is the downsampling matrix and B is the blur matrix.

For our PET reconstruction problem, the relationship between the observed projection measurements $\mathbf{g}$ and the underlying high-resolution PET image $\mathbf{f}_H$ is given by $\mathbf{g} = H_1 D\mathbf{f}_H$, where H_1 is the system matrix for low-resolution forward projection. Figure 1 shows a schematic diagram of our method to increase the pixel resolution using an HR backprojector in the process of iterative reconstruction.

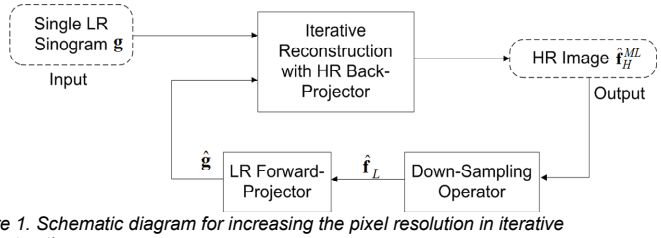

Figure 1. Schematic diagram for increasing the pixel resolution in iterative reconstruction.

When a MAP reconstruction algorithm is used in Figure 1, the prior term (or the regularization term) not only regularizes the unstable data-likelihood term due to noise, but also regularizes newly created high-resolution pixels.

Regularization for SR Reconstruction

In order to incorporate a regularizer suitable for SR reconstruction, one can consider to use conventional edge-preserving regularizers, which reflect the local spatial character of the underlying source with non-quadratic priors [1]. Unfortunately, however, these regularizers tend to produce blocky piecewise smooth regions or so-called staircase effects, which may be more significant on a finer grid in SR reconstruction. In contrast, the recently developed non-local regularizers (NLRs) are attractive in that they can preserve edges in different manner by exploiting the self-similarities of the patches ([2], [3], [4] and [5]). According to our own observations, while the local regularizers with a relatively small value of the smoothing parameter perform well in preserving fine-scale edges, they are sensitive to noise. In order to reduce noise, the smoothing parameter could be increased, which in turn will degrade the reconstruction accuracy by oversmoothing the fine scale-edges. Therefore, in order to preserve fine-scale edges as well as coarse-scale edges in SR reconstruction, the two different types of regularizers may be combined into a hybrid form in the regularization term.

The two types of the regularizers used in this work are as follows:

$$R_{NLQ}(\mathbf{f}) = \gamma_1 \sum_j \sum_{k\in\Omega_j} \frac{w_{jk}}{W_j} \phi_{QD}\left(\left\|f(\mathbf{x}_j) - f(\mathbf{x}_k)\right\|\right), \text{ with}$$
$$w_{jk} = \frac{1}{d_{jk}} \exp\left(-\frac{\left\|f(\mathbf{x}_j) - f(\mathbf{x}_k)\right\|^2}{h^2}\right) \quad (3)$$

$$R_{LNQ}(\mathbf{f}) = \gamma_2 \sum_j \sum_{k\in N_{L_j}} \phi_{LNQ}\left(f_j - f_k\right). \quad (4)$$

where $f(\mathbf{x}_j)$ is an intensity vector for the patch $\mathbf{x}_j$ centered at j, Ω_j is the search window for the pixel located at j with $W_j = \sum_{k\in\Omega_j} w_{jk}$, d_{jk} is the distance between pixels j and k, N_j is a local neighborhood of the pixel located at j, and γ_1 and γ_2 are the smoothing parameters for non-local and local regularizations, respectively. In (3), $\left\|f(\mathbf{x}_j) - f(\mathbf{x}_k)\right\| = \sqrt{\sum_{l=1}^{L}\left(f(x_{j(l)}) - f(x_{k(l)})\right)^2}$ denotes the difference between the two patches centered at j and k, where $f(x_{j(l)})$ and $f(x_{k(l)})$ denote the l-th pixels in the patches centered at j and k respectively, and L is the total number of pixels in a patch. $R_{NLQ}(\mathbf{f})$ in (3) stands for the non-local quadratic (NLQ) regularizer and $R_{LNQ}(\mathbf{f})$ in (4) stands for the local non-quadratic (LNQ) regularizer.

In this work, for the LNQ regularization term, we use the following penalty function proposed by Lange [6]

$$\phi_{LNQ}(t) = \delta^2\left[\left|\frac{t}{\delta}\right| - \log\left(1 + \left|\frac{t}{\delta}\right|\right)\right]. \quad (5)$$

By combining the two regularizers described in (3) and (4), and by using the relationship between LR image $\mathbf{f}_L$ and its corresponding HR image $\mathbf{f}_H$ described in (2), we may rewrite our reconstruction problem as

$$\hat{\mathbf{f}}_H = \arg\min_{\mathbf{f}_H}\left[-L(\mathbf{g}\,|\,\mathbf{f}_H) + \tau R_{NLQ}(\mathbf{f}_H) + (1-\tau) R_{LNQ}(\mathbf{f}_H)\right], \quad (6)$$

where $\tau \in [0,1]$ is the weighting factor which controls the balance between the NLQ and LNQ regularizers. Note that τ is a fixed and space-invariant parameter (so we call this method the space in-variant combination (SIC) method). Note also that, while $\tau = 1$ reduces the regularization term to $R_{NLQ}(\mathbf{f}_H)$, $\tau = 0$ reduces to $R_{LNQ}(\mathbf{f}_H)$. Therefore, the images reconstructed by decreasing the value of τ from 1 to 0 will gradually change the reconstruction results from an NLQ reconstruction to an LNQ reconstruction. It is then expected that there will exist an optimal value of τ yielding the most accurate reconstruction by compromising the merits of the two extreme cases.

In this work, we investigate an adaptive method of finding an optimal value of τ by noting that, while the NLQ regularizer is suitable for preserving coarse-scale edges or flat regions, the LNQ regularizer is suitable for preserving fine-scale edges. Our adaptive method determines the value of τ for each pixel based on a relative weight between the following two types of pixels. (i) the pixel in a coarse-scale edge or a flat region, (ii) the pixel in a fine-scale edge. According to our own investigations, it is useful to model τ for each pixel as a one-dimensional (1-D) function of the roughness at a pixel position. We have found an empirical method of constructing such 1-D curve from a cumulative histogram of a standard deviation (SD) image obtained from an estimated reconstruction at each iteration. Note that the SD image defined in (7) measures the roughness at the pixel position j within its neighbors and the cumulative histogram of the 2-D SD image transforms the roughness into a monotonically non-decreasing 1-D curve.

$$s(f_j) = \frac{1}{L}\sum_{j=1}^{L}\left(f(\mathbf{x}_j) - mean(f(\mathbf{x}_j))\right)^2, \quad (7)$$

where $mean(f(\mathbf{x}_j))$ is the mean value of the patch $\mathbf{x}_j$ centered at j. Since the cumulative histogram has an inverted "L" shape, it is useful for classifying a pixel into two categories ((i) and (ii)). It maps onto a large value when $s(f_j)$ is large (f_j is assumed to belong to a coarse-scale edge) and maps onto a small value when $s(f_j)$ is small (f_j is assumed to belong to a fine-scale edge). Therefore, instead of using space in-variant parameter τ, we may utilize the cumulative histogram curve of the SD image to determine the value of τ for each pixel at each iteration. In this case the minimization problem for the new method is modified as follows:

$$\hat{\mathbf{f}}_H = \arg\min_{\mathbf{f}_H}\left[-L(\mathbf{g}\,|\,\mathbf{f}_H) + R^{SVC}_{NLQ}(\mathbf{f}_H) + R^{SVC}_{LNQ}(\mathbf{f}_H)\right], \text{ with}$$

$$R^{SVC}_{NLQ}(\mathbf{f}_H) = \gamma_1 \sum_j \sum_{k\in\Omega_j} \frac{w_{jk}}{W_j}\tau(s(f_j))\phi_{QD}\left(\left\|f(\mathbf{x}_j) - f(\mathbf{x}_k)\right\|\right) \qquad (8)$$

$$R^{SVC}_{LNQ}(\mathbf{f}_H) = \gamma_2 \sum_j \sum_{k\in N_{Lj}} \left(1-\tau(s(f_j))\right)\phi_{LNQ}\left(f_j - f_k\right),$$

where $\tau(s(f_j)) = \dfrac{max - min}{MAX - MIN}(\tau^o(s(f_j)) - MIN) + min$ for the normalized cumulative histogram (NCH) curve of the SD image. Here $\tau^o(s(f_j))$ is the original cumulative histogram of the SD image. MAX and MIN are the maximum and minimum values of the cumulative histogram, respectively, and max and min are the desired maximum and minimum values of the NCH curve.

Since each term in (8) is convex, we may use the complete-data ordered subsets expectation maximization ([7] and [8]) (COSEM) algorithm and expand it to include a convex minimization method for the regularization terms. However, since our regularization terms involve a non-quadratic function, it is difficult to directly minimize (8). Here we use the separable paraboloidal surrogates (SPS) algorithm [9] for the regularization terms. In this case the surrogate functions are separable in **f** and depend only on the current estimates. Note that $\tau(s(f_j))$ in (8) is not fixed but is updated within a small range of [0, 1] at each iteration. Therefore, our COSEM-MAP reconstruction method using the SPS algorithm provides an approximated solution to (8), which is close to the true solution.

Results

To test our method, we performed 2-D simulation studies using the digital Hoffman brain and autoradiograph phantoms with two different levels of the resolution; 128×128 for LR and 256×256 for HR as shown in Fig. 1(a)(e) for the Hoffman brain phantom and in Fig. 3(a)(e) for the autoradiograph phantom, respectively. The LR phantom was derived from the original HR phantom by summing up four adjacent pixels in each high-resolution phantom to generate a corresponding pixel in the associated low-resolution phantom. The projection data were acquired using 128 bins and 128 discrete angles over 360°.

Figure 2 shows anecdotal results for both LR and HR reconstructions. For HR reconstruction, the values of γ_1 and γ_2 were independently adjusted to yield a reconstruction with the lowest percentage error (PE) of MAP-NLQ and MAP-LNQ reconstructions, respectively. We chose the smoothing parameters γ_1 and γ_2 for LR images in the same manner. Note that the HR reconstructions in (f)-(h) show better subpixel accuracy than the LR reconstructions in (b)-(d) do. Figure 2(f) shows the image reconstructed by LNQ. Note that, while the fine details are well preserved, the overall image is relatively noisy. Figure 2(h) shows the image reconstructed by using NLQ, where the edges look sharp and the noise is significantly reduced. However, it lost some of the fine details. Figure 2(g) shows the combination of NLQ and LNQ with $\tau = 0.7$ which makes the PE value a minimum, where both the fine-scale and coarse-scale edges are well preserved, which is also true for the LR reconstructions.

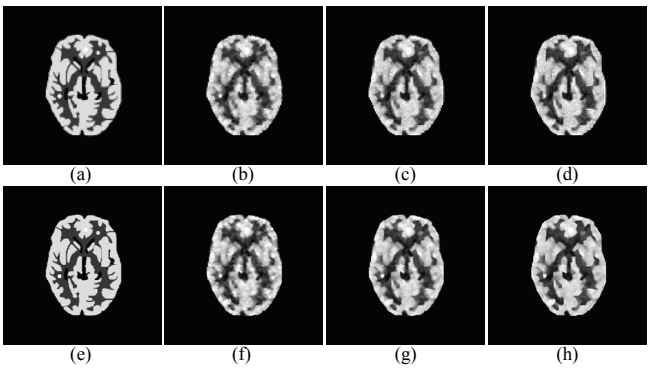

Figure 2. Hoffman brain phantoms and anecdotal COSEM-MAP reconstructions with two levels (LR and HR) of pixel resolutions: (a) LR phantom; (b) LR reconstruction using LNQ prior (PE=28.02%); (c) LR reconstruction using SIC prior with $\tau = 0.7$ (PE=27.29%); (d) LR reconstrution using NLQ (PE=27.45%); (e) HR phantom; (f) HR reconstruction using LNQ prior (PE=24.50%); (g) HR reconstruction using SIC prior with $\tau = 0.7$ (PE=23.75%); (h) HR reconstruction using NLQ prior (PE=24.42%).

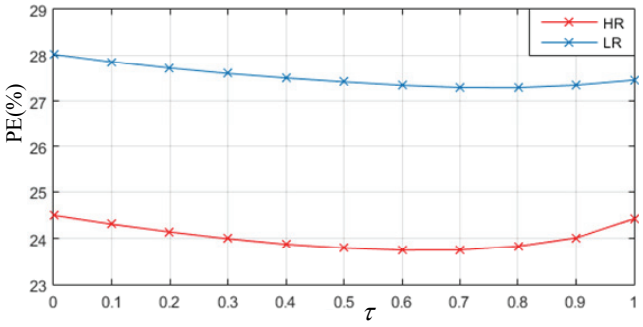

Figure 3. PE curves of Hoffman brain phantom for high- and low-resolution SIC reconstructions over a range of $\tau \in [0,1]$.

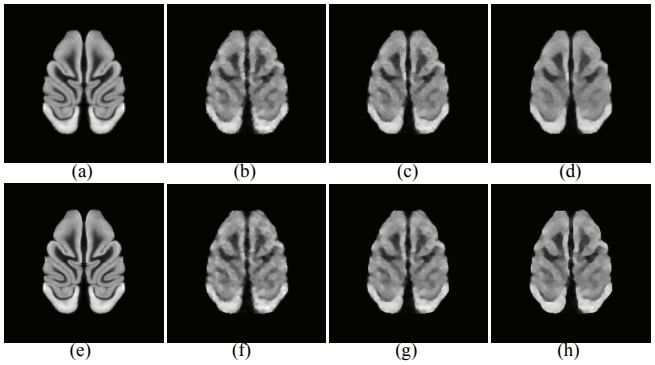

Figure 4. Autoradiograph phantoms and anecdotal COSEM-MAP reconstructions with two levels (LR and HR) of pixel resolutions: (a) LR phantom; (b) LR reconstruction using LNQ prior (PE=19.17%); (c) LR reconstruction using SIC prior with $\tau = 0.7$ (PE=18.36%); (d) LR reconstruction using NLQ prior (PE=18.87%); (e) HR phantom; (f) HR reconstruction using LNQ prior (PE=18.05%); (g) HR reconstruction using SIC prior with $\tau = 0.5$ (PE=17.77%); (h) HR reconstruction using NLQ prior (PE=18.61%).

Figure 3 shows τ versus PE curves for both LR and HR reconstructions with the Hoffman brain phantom, which indicates that both curves have the minimum of PE at the same value of $\tau = 0.7$. Notice that the HR reconstructions significantly reduce PE over the corresponding LR reconstructions.

Figure 4 shows anecdotal results of both LR and HR reconstructions for the autoradiograph phantom. Qualitative comparisons in Fig. 4 are similar to those in Fig. 2. However, $\tau = 0.5$ yields a minimal PE value for the HR reconstruction with a combination of NLQ and LNQ (See Fig. 4(g)), which indicates that different phantoms with different image roughness have different optimal τ values.

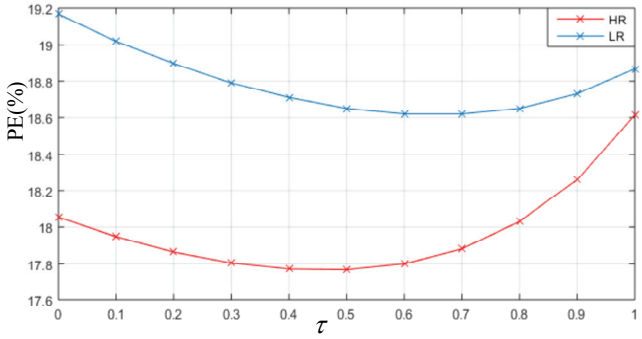

Figure 5. PE versus $\tau \in [0,1]$ curves of anecdotal COSEM-MAP-SIC reconstructions for the autoradiograph phantom with two levels (LR and HR) of resolutions.

Figure 5 shows τ versus PE curves of both LR and HR reconstructions for the autoradiograph phantom, where the curves for LR and HR reconstructions have values of $\tau = 0.7$ and $\tau = 0.5$, respectively, for the minimal PE. Similarly to Fig. 3, the HR reconstructions exhibit lower PE values than the corresponding LR reconstructions.

Figure 6 shows comparisons of SIC and SVC for both Hoffman brain and autoradiograph phantoms. Comparison of (a) and (b) shows that the adaptive SVC method provides a result very close to the one generated by the SIC method with a manually chosen optimal τ . The same is true for (c) and (d) for the autoradiograph phantom.

Figures 7 and 8 show our numerical results from the ROI studies with the reconstructions obtained from 50 independent noise trials for the Hoffman brain phantom. To measure the mean contrast recovery coefficients (MCRCs) and mean percentage errors (MPEs), we chose 11 regions that contained flat regions as well as edge regions as shown in Fig. 7(a). R1-R3 are for tumor regions. While R4-R8 were chosen across edges which include coarse-scale and fine-scale edges, R9-R11 were chosen in flat regions. Figure 7(b) shows that, in the tumor regions, the MCRCs of SIC and SVC are always in between the MCRCs of NLQ and LNQ. Figure 8 shows that NLQ has better performance in flat regions as well as coarse-scale edge regions, while LNQ performs better in fine-scale edge regions. The SIC with optimal τ compromises NLQ and LNQ methods, which not only recovers sharp edges and fine details in the edge regions, but also suppresses the noise in flat regions. In the overall comparison, the results generated by the adaptive SVC are comparable to the results generated by SIC with an optimal value of τ and also SVC well compromises NLQ and LNQ.

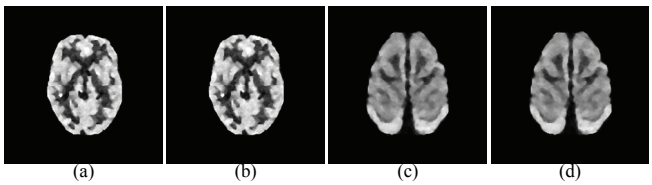

Figure 6. Comparison of SVC prior with SIC prior for HR reconstructions: (a) SVC (PE=23.76%); (b) SIC with $\tau = 0.7$ (PE=23.75%); (c) SVC (PE=17.85%); (d) SIC with $\tau = 0.5$ (PE=17.77%).

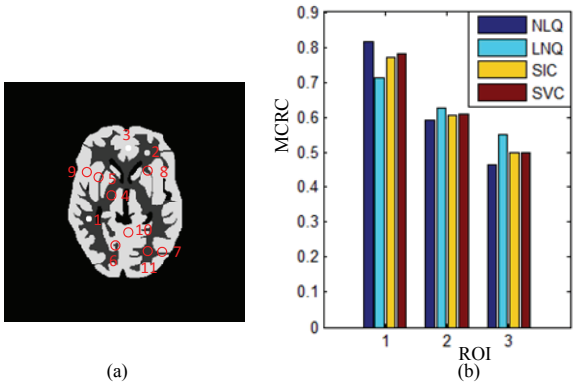

Figure 7. Comparison of MCRCs for ROIs: (a) The phantom with region borders superposed; (b) MCRCs of tumor regions (R1-R3).

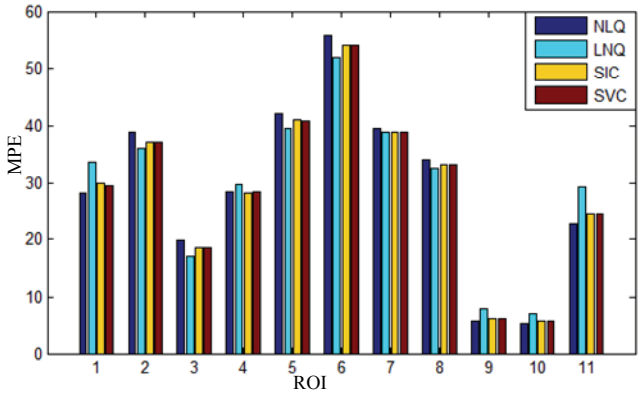

Figure 8. Comparison of MPEs of ROIs in Fig.7(a).

The regional MPE and MCRC of each ROI are defined as

$$MPE_{R_i} = \frac{1}{K}\sum_{k=1}^{K}\sqrt{\sum_{j\in R_i}(\hat{f}_j^k - f_j)^2 \Big/ \sum_{j\in R_i} f_j^2} \times 100\%, \text{ and} \tag{9}$$

$$MCRC_{R_i} = \frac{1}{K}\sum_{k=1}^{K} CRC_{R_i}^k, \text{ respectively,} \tag{10}$$

where i is the index of the ROIs, k is the index of noise realizations, and $CRC_{R_i}^k = CR_{R_i}^k / CR_{R_0}^k$ with $CR_{R_i}^k = | Z_{R_i}^k - Z_{R_B}^k | / Z_{R_B}^k$

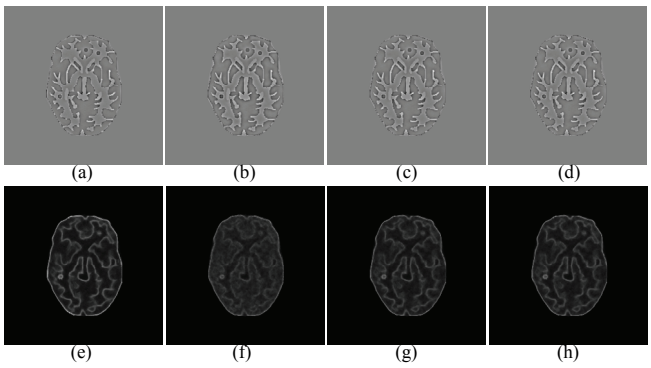

Figure 9. Point-wise bias and SD images obtained from 50 independent noise trials; (a), (b), (c) and (d) are the bias images for NLQ, LNQ, SIC with $\tau = 0.7$ and SVC respectively; (e), (f), (g) and (h) are theSD images for NLQ, LNQ, SIC with $\tau = 0.7$ and SVC, respectively.

and $Z_{R_i}^k = \frac{1}{T}\sum_{j \in R_i} \hat{f}_j^k$ denoting the mean activity in each region at the *k*-th noise trial, T the number of pixels in the *i*-th ROI, $Z_{R_B}^k$ the mean activity in the background region, and $CR_{R_0}^k$ the true contrast in the phantom.

Figure 9 shows the point-wise bias and SD images obtained from 50 independent Poisson noise trials. Comparison of the four bias images in (a)-(d) indicates that SVC as well as SIC compromises NLQ showing relatively large bias errors and LNQ showing relatively small bias errors especially around fine-scale edges. Comparison of the four SD images indicates that NLQ in (e) reveals the highest SD along the edges due to its unstable edge localization, and SIC in (g) and SVC in (h) compromise NLQ in (e) and LNQ in (f) as expected.

Conclusion

We have developed COSEM-MAP reconstruction methods that can efficiently increase the pixel resolution of PET images from a single low-resolution sinogram by using both local and non-local regularizers. The idea of increasing the pixel resolution is based on the backprojection of the low-resolution projection data into the high-resolution image space defined on a finer grid within an iterative reconstruction algorithm.

To enhance the reconstruction accuracy, we also formulated the high-resolution image constraint with both NLQ and LNQ regularizers, each of which has its own merit in preserving important features in the underlying image. The constraint was formulated by linearly combining the two regularizers in two different forms; (i) space-invariant combination (SIC) with a fixed value of τ , and (ii) space-variant combination (SVC) with a position-dependent value of τ . It is important to point out that the form in (ii) is adaptive in that the value of τ is updated at each iteration of COSEM-MAP as a function of the NCH of the SD image obtained from a previous iteration.

The net conclusion based on our experimental results is that both the SIC and SVC methods improve the reconstruction accuracy when the pixel resolution is increased on a finer grid. Moreover, while the value of τ in SIC is manually chosen, that in SVC is adaptively determined in the process of iterative reconstruction.

Acknowledgments

This work was supported by the National Research Foundation of Korea (NRF) grant funded by the Korea government (MSIP and MOE) under Grants 2014R1A2A2A01002626 and 2016R1D1A3B04933319.

References

[1] S.J. Lee, "Performance comparison of convex-nonquadratic priors for Bayesian tomographic reconstruction," Journal of Electronic Imaging, vol. 9, no. 3, pp. 242–250, 2000.

[2] A. Buades, B. Coll, and J.M. Morel, "A nonlocal algorithm for image denoising," In: Proc. IEEE Int. Conf. Computer Vision Pattern Recognition, vol. 2, pp. 60–65, 2005.

[3] A. Buades, B. Coll, and J.M. Morel, "A review of image denoising methods, with a new one," Multiscale Modeling and Simulation, vol. 4, no. 2, pp. 490-530, 2006.

[4] C. Chung, F. Roger, D.F. David, and M. Steven , "Median Non-local Means Filtering for Low SNR Image Denoising: Application to PET with Anatomical Knowledge, " IEEE Nuclear Science Symposium Conference Record (NSS/MIC), pp. 3613-3618, 2010.

[5] V. G. Nguyen and S. J. Lee, "Incorporating Anatomical Side Information into PET Reconstruction Using Nonlocal Regularization," IEEE Transactions on Image Processing, vol. 22, no. 10, pp. 3961-3973, 2013.

[6] K. Lange, "Convergence of EM image reconstruction algorithms with Gibbs smoothing," IEEE Trans. Med. Imaging MI, vol. 9, no. 4, pp. 439–446, 1990.

[7] H. Erdogan and J.A. Fessler, "Ordered subsets algorithms for transmission tomography," Phys. Med. Biol., vol. 44, pp. 2835-2851, 1999.

[8] H. Erdogan and J.A. Fessler, "Monotonic Algorithms for Transmission Tomography," IEEE Transactions on Medical Imaging, vol. 18, no. 9, pp. 801-814, 1999.

[9] I.T. Hsiao, A. Rangarajan and G. Gindi, "A new convergent MAP reconstruction algorithm for emission tomography using ordered subsets and separable surrogates," Conf. Rec. IEEE Int. Symp. Biomed. Imaging, pp. 409-412, 2002.

Author Biography

Xue Ren received the B.S. degree from Qingdao University of Science and Technology, China, in 2011 and the M.S. degree in Electronic Engineering from Paichai University, Daejeon, Korea, in 2014. She is currently pursuing the Ph.D. degree in Electronic Engineering at Paichai University, Korea. Her research interests are in image processing, computer vision and their applications to tomographic reconstruction.